International Journal of Minerals, Metallurgy and Materials
Volume 27, Number 3, March 2020, Page 401
https://doi.org/10.1007/s12613-019-1946-y

Microstructural analysis and hot corrosion behavior of HVOF-sprayed Ni–22Cr–10Al–1Y and Ni–22Cr–10Al–1Y–SiC (N) coatings on ASTM-SA213-T22 steel

Gurmail Singh[1,2], *Niraj Bala*[3], *and Vikas Chawla*[1]

1) Department of Mechanical Engineering, IKGPTU, Jalandhar 144603, Punjab, India
2) Department of Aerospace Engineering, Chandigarh University, Gharuan 140413, Punjab, India
3) Department of Mechanical Engineering, BBSBEC, Fatehgarh Sahib 140407, Punjab, India
(Received: 12 September 2019; revised: 12 October 2019; accepted: 11 November 2019)

Abstract: The present paper deals with the investigation of microstructure and high-temperature hot corrosion behavior of high-velocity oxy fuel (HVOF)-produced coatings. Two powder coating compositions, namely, Ni22Cr10Al1Y alloy powder and Ni22Cr10Al1Y (80wt%; micro-sized)–silicon carbide (SiC) (20wt%; nano (N)) powder, were deposited on a T-22 boiler tube steel. The hot corrosion behavior of bare and coated steels was tested at 900°C for 50 cycles in Na_2SO_4–60wt%V_2O_5 molten-salt environment. The kinetics of corrosion was established with weight change measurements after each cycle. The microporosity and microhardness of the as-coated samples have been reported. The X-ray diffraction, field emission-scanning electron microscopy/energy dispersive spectroscopy, and X-ray mapping characterization techniques have been utilized for structural analysis of the as-coated and hot-corroded samples. The results showed that both coatings were deposited with a porosity less than 2%. Both coated samples revealed the development of harder surfaces than the substrate. During hot corrosion testing, the bare T22 steel showed an accelerated corrosion in comparison with its coated counterparts. The HVOF-sprayed coatings were befitted effectively by maintaining their adherence during testing. The Ni22Cr10Al1Y–20wt%SiC (N) composite coating was more effective than the Ni–22Cr–10Al–1Y coating against corrosion in the high-temperature fluxing process.

Keywords: high-velocity oxy fuel; thermal spray; hot corrosion; oxide scale; nano-structured coating

1. Introduction

High-temperature corrosion process is an uncompromising problem in the energy generation boilers and gas turbines. This problem worsens with the use of low-grade fuel oils and fossil fuels. The flue gases produced by low-grade fuels cause the accelerated degradation process of materials, i.e., hot corrosion or corrosion in the liquefied salt environment [1–2]. The elevated-temperature gaseous environment of boilers comprises various influential elements, such as sodium (Na), sulfur (S), and vanadium (V), which produce a thin film of fused salt over the parts [3]. Normally, the deposition of mixture of sodium sulfate (Na_2SO_4) and vanadium pentoxide (V_2O_5) melt is evident on different boiler parts. The mixing of Na_2SO_4 and 60wt% V_2O_5 results in the conglomeration and formation of sodium metavanadate ($NaVO_3$), which features a low melting point (610°C); however, a eutectic reaction could occur at a lower temperature. Ultimately, the establishment of this melt over various boiler parts promotes the accelerated degradation of applicable materials, thus shortening the lifespan of parts and later causing catastrophic failure [4–6].

Numerous studies showed that the thin and dense deposited coatings made with metallic, ceramic, and composite powders have provided resistance against high-temperature oxidation and corrosion. With regard to deposition, the thermal spray coating technology is one of the cutting-edge ways to deposit protective coatings [7–8]. Various spraying alternatives, such as detonation gun spray, plasma spray, high-velocity oxy fuel (HVOF) spray, and cold spray tech-

Corresponding author: Gurmail Singh E-mail: gurmail.malhi@gmail.com

nique, are available. The HVOF spray is an advantageous thermal spray system that is usually utilized in a number of industries owing to its flexibility and economical price. The coatings yielded by HVOF method possess desirable properties, including low porosity, high hardness with increased binding strength, and low level of decarburization, compared with its alternative deposition approaches [9–10].

In coated surfaces, MCrAlY (M = Ni, Co, both) coatings are popular oxidation/corrosion-resistant coatings used to shield materials from harmful high-temperature oxidation and hot corrosion attack [11–12]. In earlier studies, the performance of NiCrAlY coatings was improved by the addition of reinforcement ceramics and hard materials, such as Al_2O_3 [13], SiN [14], CrN, or CrON [15]. The existence of carbides in coatings has led to an improvement in the coating performance, for example, adherence, corrosion, and tribological properties [15–18]. Specifically, the addition of silicon carbide (SiC) is used to boost the mechanical and tribological properties of coatings [19–20]. SiC-based coating composition, which enables surface improvement by boundary lubrication for wear-accelerated corrosion applications, has been used to develop SiO_2 compounds [21]. The glassy SiO_2-rich layer is considered a protective barrier against the inward diffusion of oxygen [22]. SiC coating is considered to possess self-healing property, which enhances the oxidation resistance and spallation resistance of thermal barrier coating systems [23]. In NiCrAlYSiN- and NiCrAlYSi-based composite coatings, the presence of Si exhibited desirable results in hot-corrosion applications [14].

The size of powder granules plays a vital role in surface coating. Nano-sized powder coating performance characteristics, namely, density, surface hardness, anti-corrosion, and tribological properties, are better compared with those of microparticle coatings [24–27]. Nanocoatings possess a surface with tremendously high-density grain boundaries, which develop from nonporous coatings. The high-energy ball milling method is used to achieve nanocomposite or nano-structured powders [28–29]; *in situ* amalgamation in a matrix becomes evident in powder blends by mechanical milling.

The present study aimed to investigate the comparative hot corrosion behavior of novel NiCrAlY–20wt%SiC (nano (N)) composite coating, NiCrAlY alloy coating, and bare material of the substrate. Both coatings have been deposited by HVOF thermal spray method on a T22 steel. Subsequently, the microstructure and high-temperature corrosion behavior was examined in a molten-salt environment at elevated temperature of 900°C in a cyclic study of 50 cycles.

2. Experimental

2.1. Substrate material and feedstock powder

An Fe-based alloy steel designated as ASME-SA213-T-22 (Grade T22) has been utilized as the substrate for coating deposition. T-22 alloy is a useful tube steel in power plants in India. The chemical composition of the steel has been analyzed with an optical emission spectrometer (ThermoJarrel Ash, TJA 181/81, USA). Table 1 provides the chemical composition of the alloy. Rectangular-shaped specimens with approximate dimensions of 20 mm × 10 mm × 5 mm were cut from the tubes. The samples were cleaned ultrasonically, dried, mirror-polished, and sand-blasted prior to coating deposition. Two powders (Ni–22Cr–10Al–1Y and nano-SiC) were selected for deposition. Figs. 1 and 2 depict the field

Table 1. Chemical composition of ASME-SA213-T22 boiler tube steel wt%

C	Cr	Mn	Ni	S	P	Si	Mo	V	Fe
0.14	2.65	0.17	0.016	0.01	0.02	0.45	1.06	0.005	Bal.

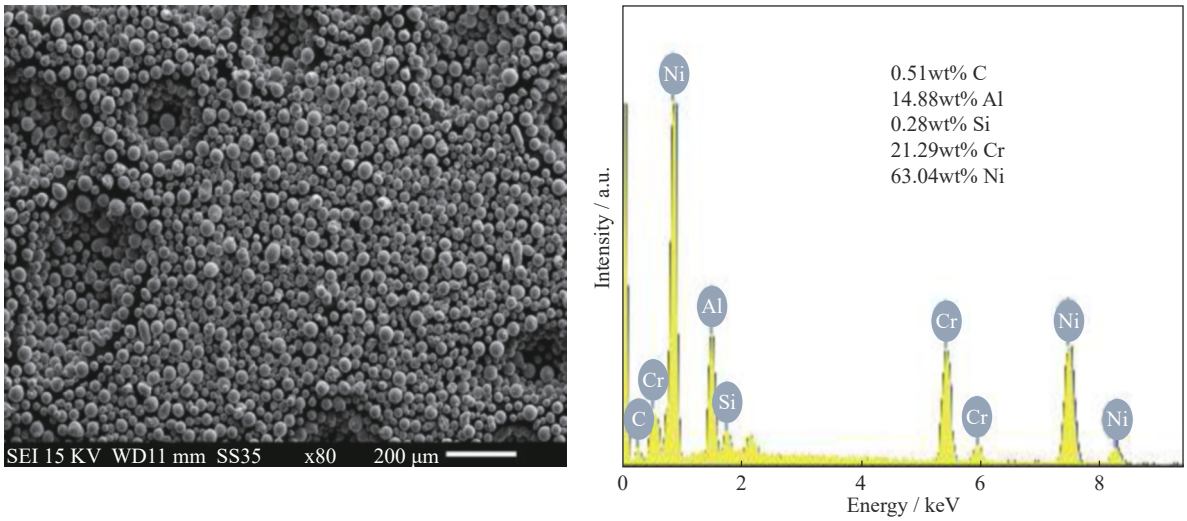

Fig. 1. SEM/EDS analysis of Ni22Cr10Al1Y powder.

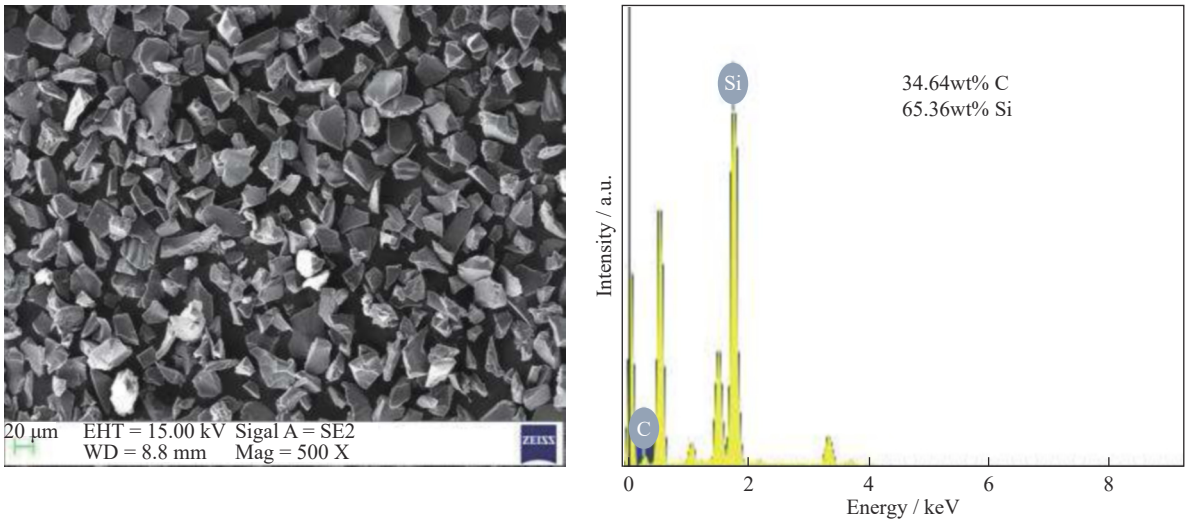

Fig. 2. SEM/EDS analysis of SiC powder before milling.

emission-scanning electron microscopy/energy dispersive spectroscopy (FE-SEM/EDS) of the two powders. Two powders Ni–22Cr–10Al–1Y (Praxair Ni-343) and nano-SiC having different particle sizes were mixed to produce a composite coating. The nano-sized SiC powder was attained by ball milling. The nano-carbide powder particles were characterized with FE-SEM/EDS (Fig. 3) and transmission electron microscopy (TEM)/EDS analyses (Fig. 4). The composite powder blend was achieved by high-energy ball milling machine. The particulars of the powders are detailed in Table 2.

2.2. Development of coatings

The substrate samples were grit-blasted with Al_2O_3 (grit: 60) by an abrasive blasting machine to achieve good coating adherence. The roughened specimens with roughness R_a in the range of 5.75–6.15 µm were prepared. The coatings were prepared by a HVOF thermal spray system fitted with HIPOJET-2700 apparatus (Metallizing Equipment Pvt. Co., Ltd., Jodhpur, India). The thickness of coatings was maintained approximately in the range of 120–130 µm during deposition. The temperature of substrate steels was maintained by cooling with compressed air jets during and after spraying to restrict unnecessary phase changes. The HVOF process parameters were kept constant during the deposition process. Table 3 lists the HVOF process parameters.

2.3. Porosity and microhardness measurements

The microporosity was investigated by the image processing software ImageJ using the surface SEM micrograph. The average values of 10 readings for porosity have been re-

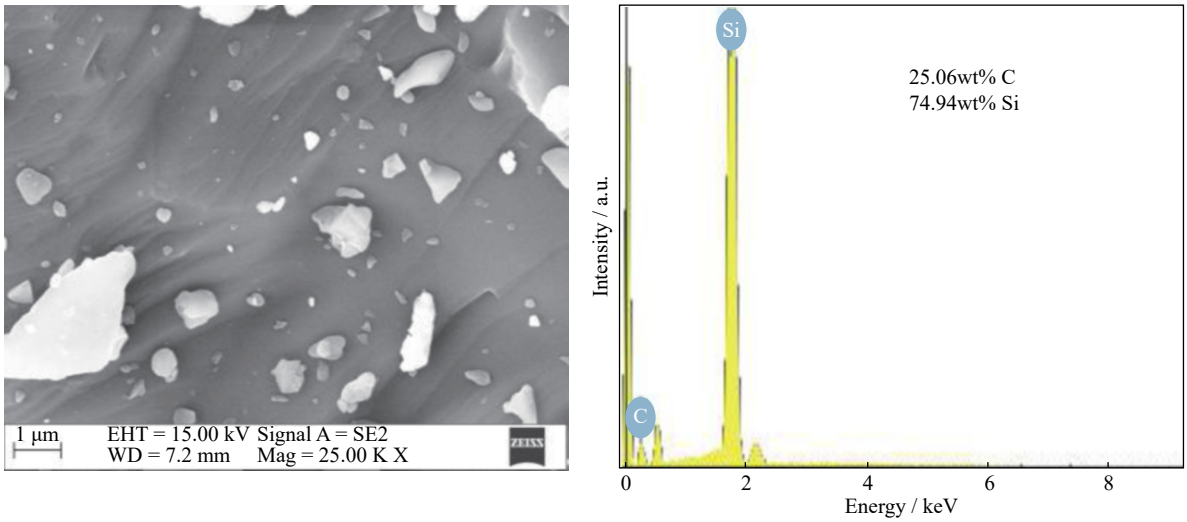

Fig. 3. SEM/EDS of milled nano-SiC powder.

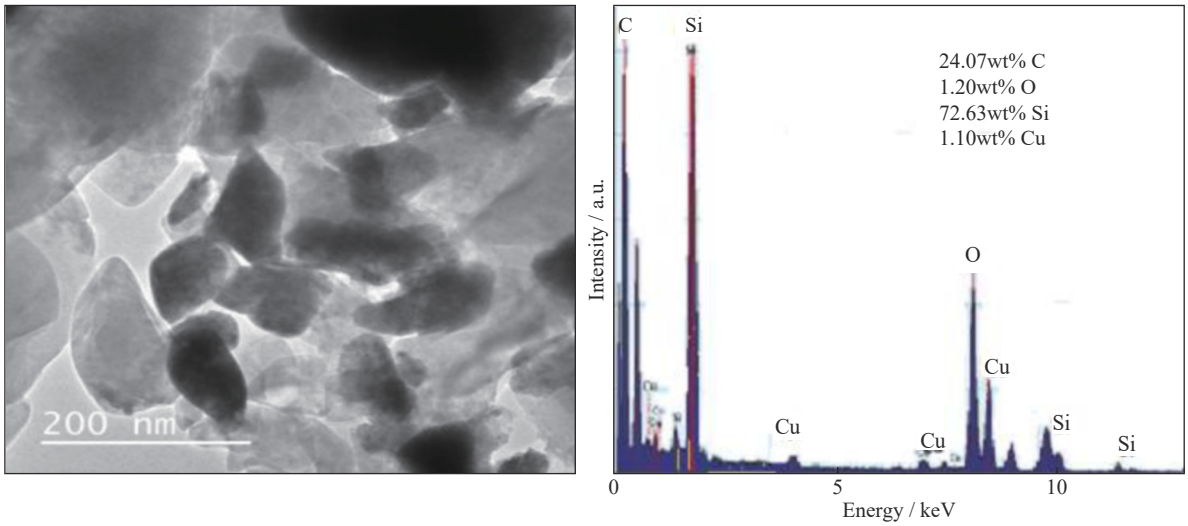

Fig. 4. TEM/EDS analysis of milled nano-SiC powder.

Table 2. Composition details of feedstock powders

Feedstock powder	Composition	Particle size
Ni–22Cr–10Al–1Y Powder	Cr (22wt%), Al (10wt%), Y (1wt%), Ni (Bal.)	38 ± 5 μm (400 Mesh)
Ni–22Cr–10Al–1Y–20SiC (N) composite Powder	80wt% of {Cr (22wt%), Al (10wt%), Y (1wt%), Ni (Bal.)} and 20wt% SiC	Blend of Ni–22Cr–10Al–1Y 38 ± 5 μm and milled SiC (99% pure) nano powder (with approx. carbides size 100 nm)

Table 3. HVOF process parameters

Oxygen flow rate / ($L \cdot min^{-1}$)	250
Fuel (LPG) flow rate / ($L \cdot min^{-1}$)	60
Air-flow rate / ($L \cdot min^{-1}$)	700
Spray distance / cm	20
Powder feed rate / ($g \cdot min^{-1}$)	30–38
Fuel pressure / MPa	0.6
Oxygen pressure / MPa	0.8
Air pressure / MPa	0.6

ported. The microhardness measurements had been carried out along the cross-section of samples with a digital micro Vickers hardness tester.

2.4. Molten-salt corrosion test

Hot corrosion studies were executed in a molten-salt environment by pasting Na_2SO_4–60wt%V_2O_5 paste on the coated and uncoated specimens. The amount of salt coating was kept in the range of 4.0–5.0 mg/cm^2. The samples were dried after salt pasting. Subsequently, cyclic studies were carried out with heating in a SiC tube furnace (Digitech, India) for 1 h followed by 20 min cooling at room temperature in ambient air. The experiment was conducted for 50 cycles. The furnace was calibrated by using a platinum–rhodium thermocouple (Electromek, India) and a temperature indicator with an error of ±5°C. The samples were positioned in the furnace tube by employing alumina boats. The boats were pre-heated at 450°C for 4–5 h prior to use. The relative mass and physical changes were noted to establish the corrosion kinetics. For surface area calculation, the samples borders were measured with a digital vernier caliper (Mitutiyo, Japan).

2.5. Thermogravimetric studies

In the thermogravimetric studies, the measured mass changes per unit surface area were plotted against the number of cycles. The square of mass changes per unit surface area graph was plotted to access the regression fitness of weight loss during hot corrosion.

2.6. Characterization of coating

As-coated and corroded surfaces were characterized by various techniques, such as X-ray diffraction (XRD) analysis and FE-SEM/EDS. The cross-section morphologies of the as-coated and corroded surface samples were also checked observed by FE-SEM/EDS analysis and EDS mapping analysis. The samples were sectioned and mounted in epoxy rings prior to characterization.

3. Results

3.1. As-sprayed coatings results

3.1.1. Microporosity and microhardness of deposited coatings

The HVOF technique has yielded extremely dense and uniform coatings with thicknesses in the range of approxim-

ately 120–130 μm after deposition. The as-coated HVOF surfaces appeared in silver gray color. The microhardness of T22 steel ranged as HV 156–256. Table 4 lists the porosity and microhardness results of coatings.

Table 4. Characteristics of as-sprayed coating

Coating	Designation	Porosity	Hardness, HV
Ni–22Cr–10Al–1Y	NiCrAlY	1.64%–1.7%	558–614
Ni–22Cr–10Al–1Y20SiC (N)	NiCrAlY–20wt%SiC (N)	0.95%–0.97%	766–776

3.1.2. XRD result of as-sprayed coatings

The XRD result of the as-coated NiCrAlY surface (Fig. 5) primarily consists of intermetallic compounds similar to the powder composition elements, i.e., nickel, chromium, and aluminum-based phases (Ni_3Al, NiAl, and Ni_3Cr_2). Correspondingly, the XRD analysis of as-coated NiCrAlY–20wt%SiC (N) surface also showed the formation of intermetallic compounds of nickel, aluminum, and chromium together with the SiC phase. Small peaks of iron–nickel (Ni–Fe) were also evident.

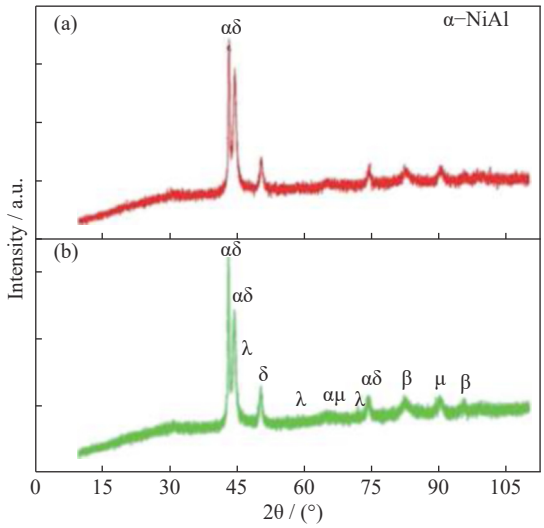

Fig. 5. XRD analysis of (a) Ni22Cr10Al1Y coating and (b) Ni22Cr10Al1Y–20wt%SiC (N) composite coating.

3.1.3. SEM/EDS results of as-sprayed coatings

Fig. 6 illustrates the classical surface morphology of HVOF coatings. Fig. 6(a) shows the microstructure of NiCrAlY alloy coating formed with un-melted, fully melted, and partially melted particle splats. At specific sites, very fine, fragmented, and deformed particles were also evident. Limited superficial voids were detected over the entire surface. The coatings were shaped by the overlapping splats. In EDS analysis, NiCrAlY-coated surface elements, such as Ni, Cr, and Al, were substantially present along with the negligible content of Y. After the addition of SiC (N), the number of un-melted particles in NiCrAlY coating has significantly reduced, and the coatings showed a refined and dense microstructure with less number of voids (Fig. 6(b)). Moreover, the coating surface was smoother than the previous one. The EDS analysis of NiCrAlY–20%SiC (N) composite coating showed the adequate presence of Si particles with C particles along with all other powder composition particles. The small amounts of carbon and oxygen indicate the development of carbides of Si or Cr and localized oxides of Al, Si, Cr, and Ni on the coating surface.

3.1.4. Cross-sectional analysis results of the as-sprayed coatings

The average thickness of NiCrAlY coating was around 119 μm as measured from the cross-sectional SEM analysis (Fig. 7(a)). The overall coating–substrate interface was laminar, dense, tightly packed, and adherent. Further, EDS examination at different points showed the presence of the main elements, including Ni, Al, and Cr. Limited traces of Y and Fe have also been observed. The existence of oxygen represents the possibility of oxide formation. In the EDS mapping analysis (Fig. 8(a)), the coating appeared complete with the distribution of all powder particles, including Ni, Cr, Al, and Y, and low O content. The concentration of Ni-rich particles reached the maximum, followed by Cr- and Al-rich particles. The inclusive particle distribution exposed the creation of intermetallic compounds and several oxides on the coated surface.

In the case of NiCrAlY–20wt%SiC (N), the coating layer thickness approximated 116 μm (Fig. 7(a)). The coating presented a smooth and dense structure consisting of splats stacked parallel to the interface. The EDS analysis showed the presence of Ni, Cr, Al, and Si as key elements. The existence of carbon and oxygen represents the formations of carbides and oxides, respectively, in the coating region. The EDS mapping (Fig. 8(b)) results depict the existence of all elements of the coating powder and their distribution. The coating primarily comprised Ni- and Cr-rich splats. A low amount of Al-rich splat was visible in the coating. Si was uniformly distributed and appeared dense in the coating–substrate interface region.

3.2. Hot corrosion study results

3.2.1. Thermogravimetric changes

The coated and uncoated T-22 substrates were visually

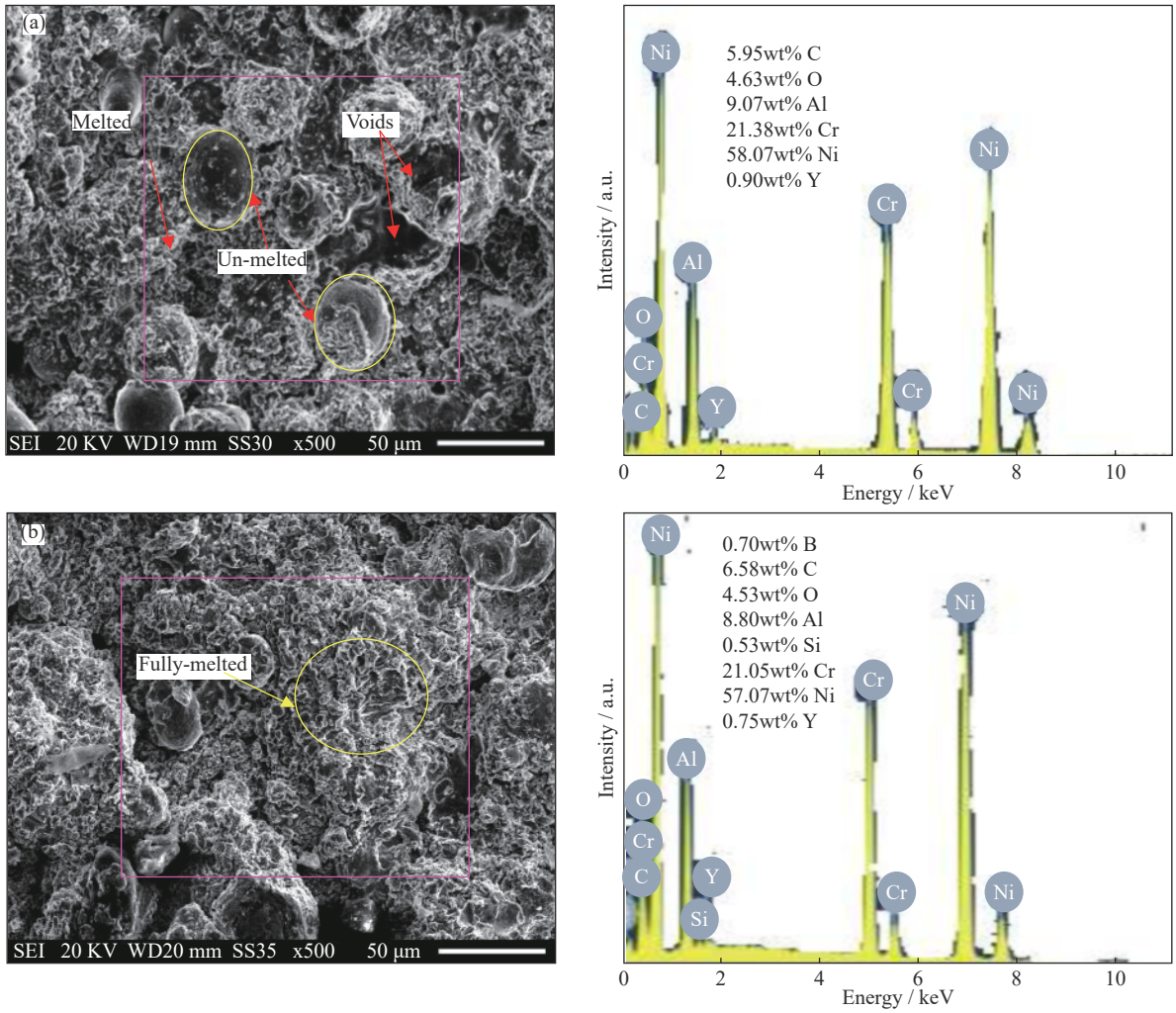

Fig. 6. SEM/EDS analysis of (a) Ni22Cr10Al1Y coating and (b) Ni22Cr10Al1Y–20%SiC (N) composite coating.

examined for weight and color changes for 50 cycles at 900°C in molten-salt environment. The uncoated T22 substrate material was spalled and peeled off severely with popping (cracking sound), the material degraded in the form of thin chips, and considerable mass gain occurred (Fig. 9(d)). Initially, at the end of the 2nd cycle, material removal was observed in the form of tiny flakes. This degradation process continued in the overall process until the 50th cycle. The weight of uncoated T22 substrate increased infinitely through the hot corrosion course. The material damage mechanism was crack formation on the topmost layer surface, followed by the disintegration of material in the form of flakes. Black and rust colors appeared from the 9th to 25th cycle.

The NiCrAlY-coated sample showed no spallation. Notable small changes in weight were noticed. After the 8th cycle, the specimen color changed from silver to gray. At the end of the 9th cycle, the color changed from gray to green, and an increase in mass was observed. The weight gain in coating continued until the 16th cycle, and it stabilized afterward. Then, the sample color turned partially brown. After the 28th cycle, black dots appeared at the surface of certain regions. After completion of process, the tested sample was obtained, as shown in Fig. 9(e).

The color of NiCrAlY–20wt%SiC (N)-coated sample changed from silver to gray after the first five cycles. The paste had reacted with the coating compounds. Several black spots were also observed after the 9th cycle. The color further converted to green with several black spots. However, no material spallation was detected during the whole study (Fig. 9(f)).

3.2.2. Weight change kinetics during hot corrosion

Fig. 10 shows the plot of mass change data per unit surface area (mg/cm^2) during hot corrosion. The cumulative mass change after 50 cycles was 217.35 mg/cm^2 for uncoated T22, 13.08 mg/cm^2 for NiCrAlY alloy coating, and 1.85 mg/cm^2 for NiCrAlY–SiC(N) composite coating. The

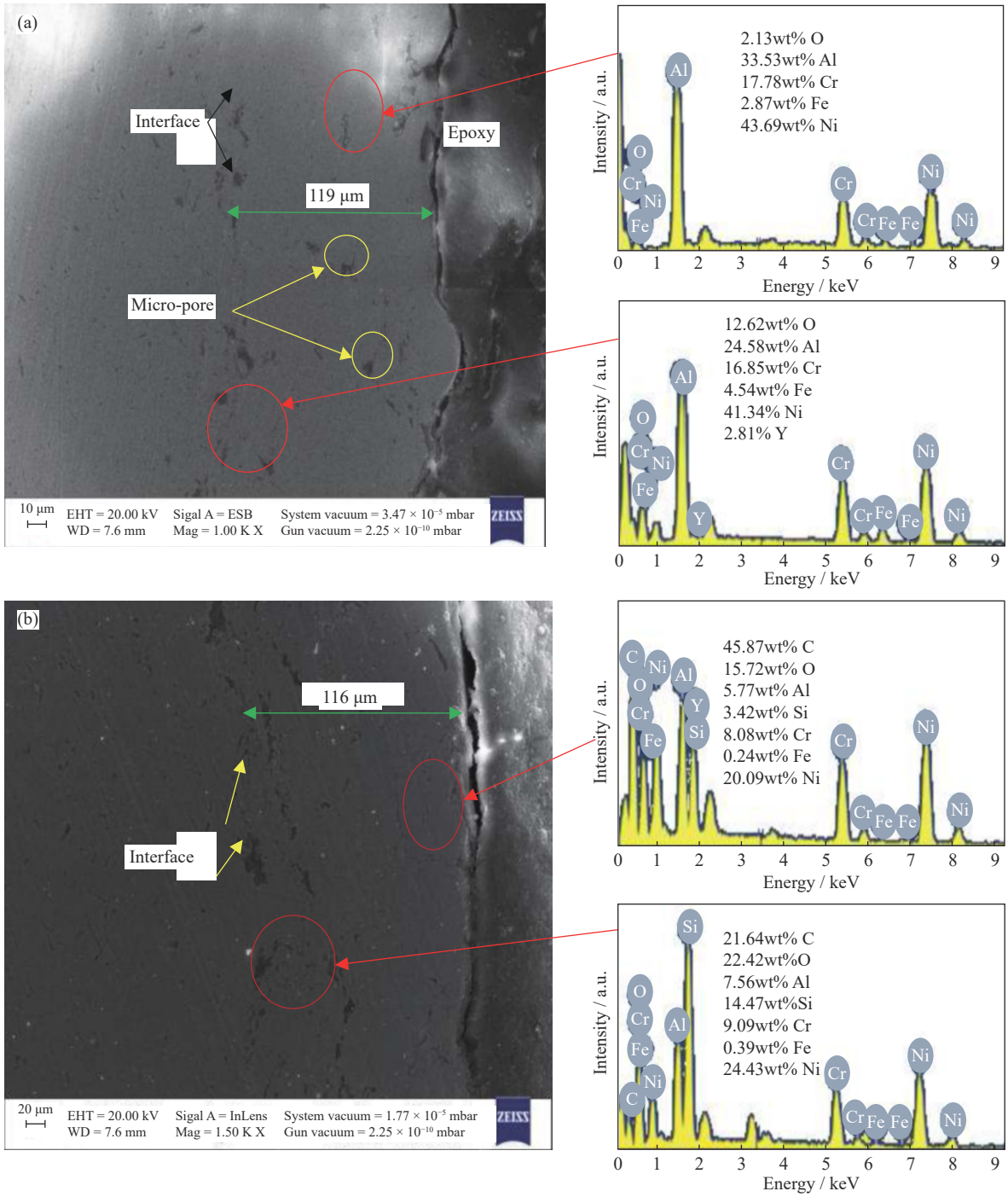

Fig. 7. Cross-sectional SEM micrograph along with EDS analysis of as-sprayed (a) Ni22Cr10Al1Y and (b) Ni22Cr10Al1Y–20wt%SiC (N) composite coating.

mass changes for the NiCrAlY coating was reduced by 93.98% compared with the uncoated counterpart. Similarly, NiCrAlY–SiC (N) composite coating exhibited a reduced mass gain of 99.15%. Fig. 11 shows the plot of square weight change per square surface area (mg^2/cm^4) for the coated and uncoated specimens followed hot corrosion. Parabolic rate constant (K_P) values have been calculated from the fitted linear regression curves for all the cases. A transition in the K_p value from 11×10^{-8} to 34.35×10^{-8} $g^2 \cdot cm^{-4} \cdot s^{-1}$ (34th cycle) was observed in the case of T22 steel. The K_p values were 0.1097×10^{-8} $g^2 \cdot cm^{-4} \cdot s^{-1}$ for NiCrAlY and 0.00089×10^{-8} $g^2 \cdot cm^{-4} \cdot s^{-1}$ for NiCrAlY–SiC (N) coating. The K_p values for the T-22 boiler steel have reduced significantly after the coating deposition.

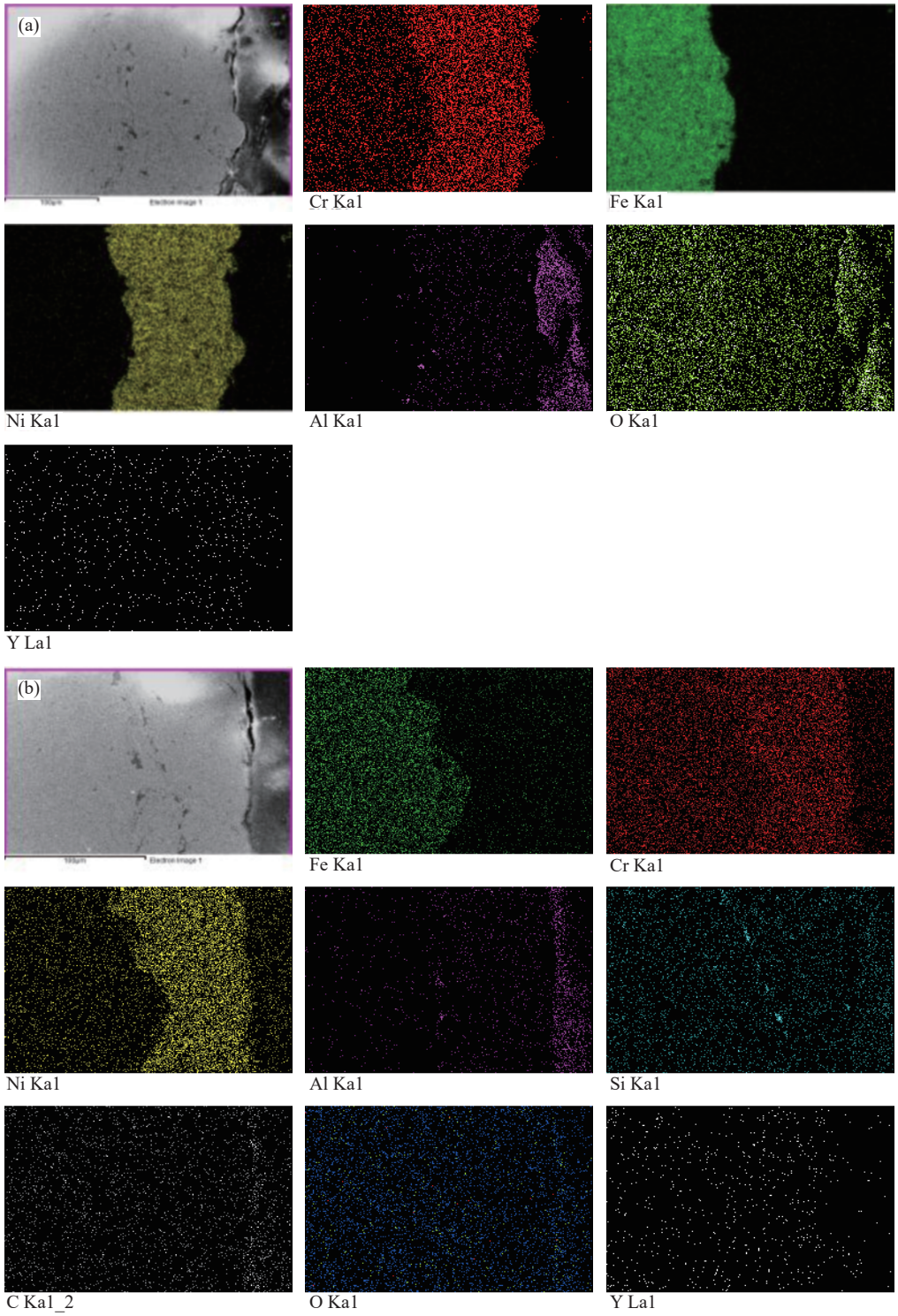

Fig. 8. EDS mapping of as-sprayed (a) Ni22Cr10Al1Y coating and (b) Ni22Cr10Al1Y–20wt%SiC (N) composite coating.

3.3. Characterization of corroded samples

3.3.1. XRD analysis of corroded samples

The XRD graph (Fig. 12(a)) of hot-corroded uncoated T-22 boiler tube steel exhibited the formation of iron(III) oxide (Fe_2O_3) scale. Fe_2O_3 was a blistering and porous scale. The metal developed rust, and after several cycles, the scale layer peeled off, which steered the accelerated corrosion rate. The XRD pattern (Fig. 12(b)) of hot-corroded NiCrAlY-coated T-22 steel consisted of oxides of Al_2O_3, spinels Ni(Cr or Al)$_2O_4$, Cr_2O_3, and NiO. The diffractogram results (Fig. 12(c)) of corroded NiCrAlY-SiC(N) composite powder-

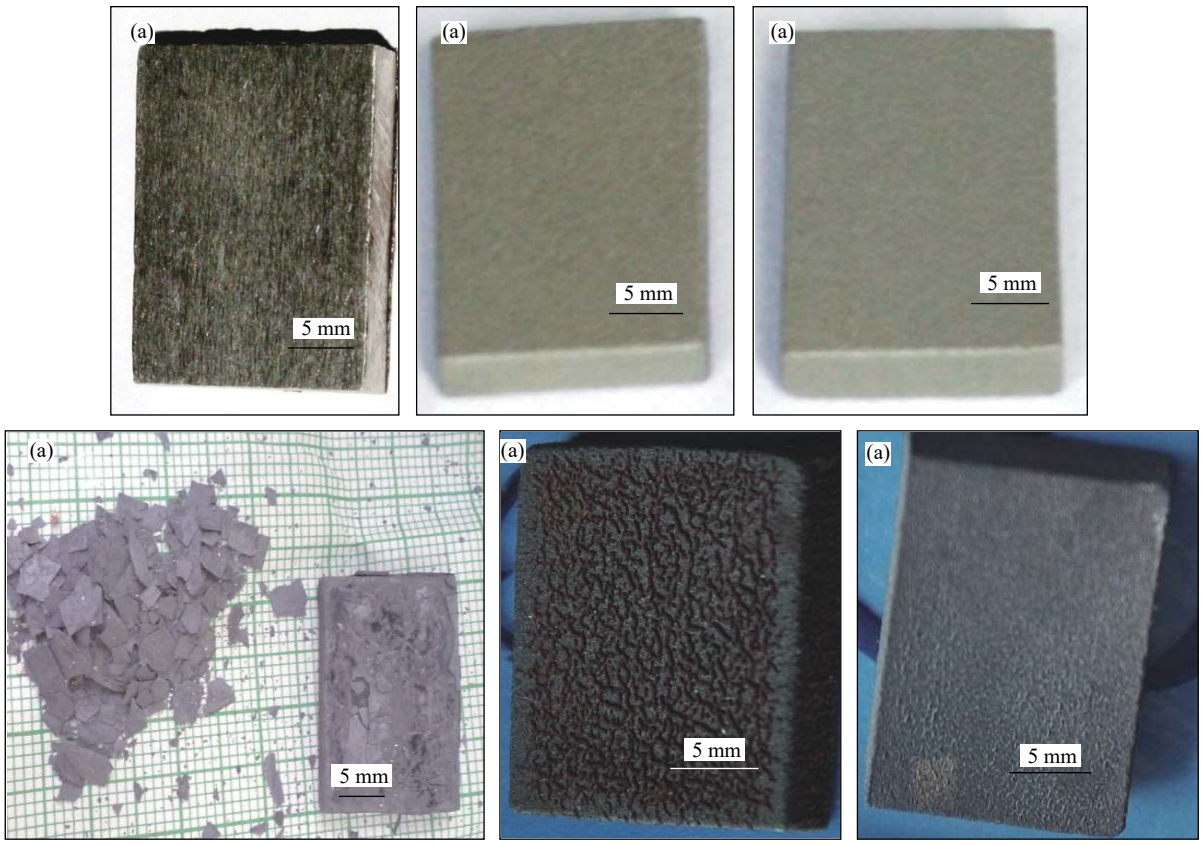

Fig. 9. Macrograph of (a) uncoated T22, (b) NiCrAlY, (c) NiCrAlY–20wt%SiC (N) powder-coated T22 steel before corrosion, and (d) uncoated T22, (e) NiCrAlY, and (f) NiCrAlY–20wt%SiC (N)-coated T22 steel after 50 cycles of hot corrosion.

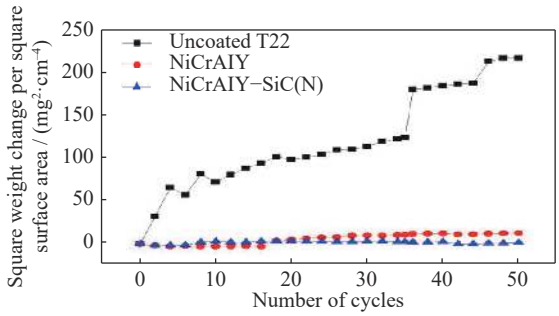

Fig. 10. Plot of square of mass change per unit area with respect to the number of cycles.

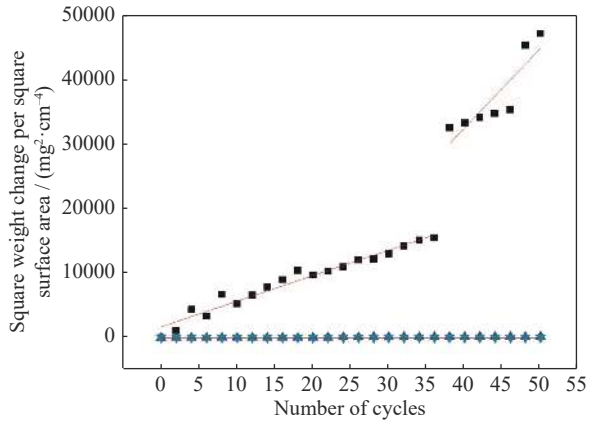

Fig. 11. Plot of square of mass change per unit area with respect to the number of cycles.

coated T-22 showed Al_2O_3, spinels Ni(Cr or Al)$_2O_4$, Cr_2O_3, and NiO compounds of alloy coating alongwith SiO_2 formation. The molten-salt paste compounds of Na and S were eliminated after corrosion of the top surface.

3.3.2. SEM/EDS analysis of corroded samples

The FE-SEM micrograph in Fig. 13(a) presents the top surface morphology of the corroded T22 steel after hot corrosion cyclic testing for 50 cycles. The surface micrograph revealed the surface with a seriously damaged oxide scale due to momentous spalling of its upper layers. The thermal cycle testing with Na_2SO_4–60wt%V_2O_5 at 900°C promoted fluxing. The exposed areas of the scale at one point appeared with columnar particle growth, and a porous scale formed at another point. The EDS analysis revealed that the scale was rich with Fe and O particles, indicating the possibility of Fe_2O_3 formation.

In the case of both coated surfaces, the SEM micrograph showed the rough morphology of the protective oxide that developed over the whole surface. The structure of both

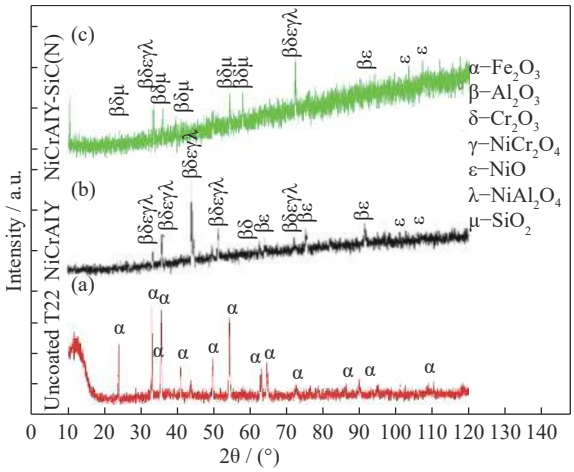

Fig. 12. XRD analysis of corroded (a) uncoated T22, (b) NiCrAlY, and (c) NiCrAlY–20wt%SiC (N)-coated T22 steel after 50 cycles of hot corrosion.

coatings indicated that inter-granular corrosion occurred due to the precipitation of intermetallic and carbide phases along the grain boundaries. Several microcracks and microporosity were observed in NiCrAlY-coated surfaces (Fig. 13(b)). The EDS analysis result on a selected point on the upper layer in the microstructure coating showed the dominance of Ni and O packed with irregularly shaped white crystals, whereas EDS analysis of another point indicated the co-presence of Ni-, Cr-, and O-rich regions at the exposed spongy underlayer of the coating. With the presence of O along with Ni, Cr, Al, and Y, compound phases, including NiO, Al_2O_3, and Cr_2O_3, may be expected. Likewise, low carbon content might lead to the formation of carbide in the coating materials. The SEM micrograph of hot-corroded NiCrAlY–SiC (N) composite coating (Fig. 13(c)) showed the presence of Si, C, and O along with other coating powder particles. The formation of additional compounds (SiO_2 and SiC) was expected to occur in the oxides of composite coatings. The Na and S phases were absent in the coated specimens.

3.3.3. Cross-sectional SEM/EDS analysis and X-ray mapping of corroded samples

The cross-sectional SEM of uncoated steel (Fig. 14(a)) showed a cracked and layered structure oxide that formed over the substrate. A prevalent corrosion attack appeared parallel to the interface of the scale/substrate because of the loosely bound oxide scale layer. EDS analysis at different levels of the oxide layer revealed the formation of iron oxide. The formation of chorium oxides was also noticed at certain depths in the subsurface. Furthermore, EDS mapping analysis (Fig. 15(a)) of uncoated T-22 steel showed the homogeneous mixture of Fe and O, indicating that the upper surface was degraded because of iron oxide formation. The dispersion of Cr and Mo has also been observed. The NiCrAlY-coated surface (Fig. 14(b)) showed the formation of tightly packed oxide scale parallel to the substrate surface near the substrate/coating interface, but the upper layers experienced a corrosion attack, and part of the coating was depleted. The upper layer consisted of Cr- and Ni-rich scale along with O, which indicated the formations of Cr_2O_3, CrO, and NiO. However, in the subscale region, Al was dominated with O, which could form Al_2O_3. Additionally, EDS mapping analysis (Fig. 15(b)) of the coating showed that Ni, Cr, and Al dominated the overall layers of the coated region. The coating/substrate interface contained dense Al, and Ni- and Cr-rich particles were packed in the overall structure of coating. NiO, Cr_2O_3, and Al_2O_3 had formed. The cross-section morphology of NiCrAlY–SiC(N) (Fig. 14(c)) showed that the top layers of the coating had successfully tolerated the corrosion attack. Different compounds, such as NiO, Cr_2O_3, and Al_2O_3, developed in the upper layers of the coating scale. The EDS mapping result (Fig. 15(c)) of NiCrAlY–SiC (N) coating showed a dense scale with Cr-, Ni-, and Al-rich splats at alternating positions. Si and C clustered at different points in the coating region. NiO, Cr_2O_3, Al_2O_3, SiO_2, and MoO formed in the overall coating. The negligible presence of C has been noted. Y was dispersed on the overall surface. Finally, X-ray mapping results showed Na and S compounds, whose levels became negligible after the corrosion.

4. Discussion

The alloy powder NiCrAlY and composite powder NiCrAlY–20wt%SiC (N) were deposited successfully by HVOF thermal spray process on a T22 boiler tube steel. The coatings with thicknesses of 115–120 μm presented a dense surface with limited porosity. NiCrAlY and NiCrAlY–20wt%SiC (N) coatings exhibited maximum hardness values of HV 614 and 776, respectively. The development of intermetallic compounds of nickel, chromium, and aluminum were obtained over the deposited NiCrAlY coating. The formation of these compounds during the deposition process occurred through the resulting reactions [30].

$$Al + Ni \rightarrow NiAl \quad (1)$$

$$Al + 3Ni \rightarrow Ni_3Al \quad (2)$$

$$3Ni + 2Cr \rightarrow Ni_3Cr_2 \quad (3)$$

The composite coating NiCrAlY–20wt%SiC (N) exhibited the formation of intermetallic compounds along with SiC. Slight oxidation of feedstock powder particles was also noticed. Limited oxidation, low porosity, and several phase transformations were observed by earlier researchers during the HVOF spray deposition process [31–33]. The micro-

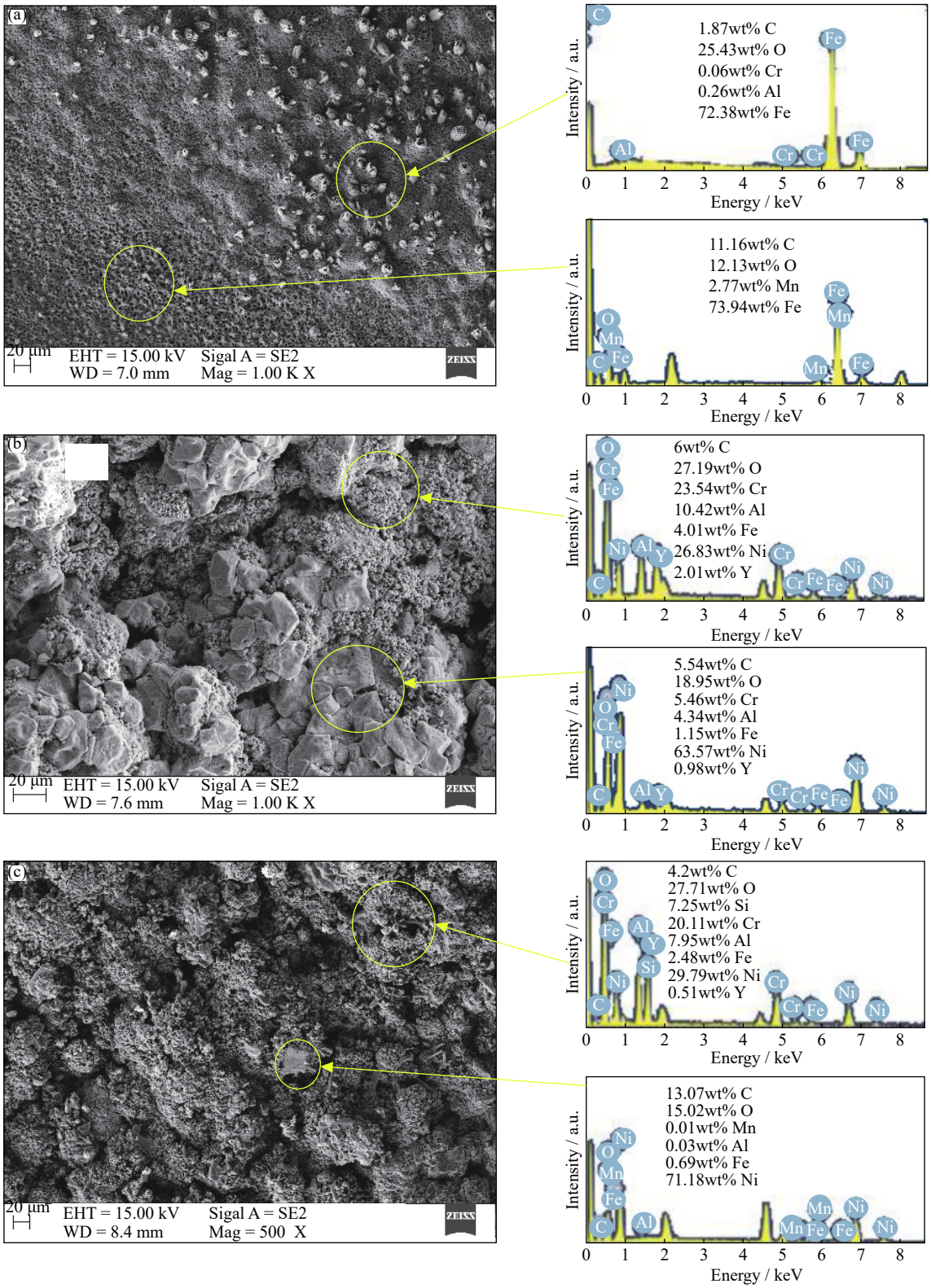

Fig. 13. SEM/EDS of corroded (a) uncoated T22, (b) NiCrAlY, and (c) NiCrAlY–20wt%SiC (N)-coated T22 steel after 50 hot corrosion cycles.

structure of typical HVOF coatings comprising fully and partially melted phases was determined. Flattening of particles after striking the substrate was also noted (Figs. 6 and 7). The EDS mapping analysis of NiCrAlY coating (Fig. 8(a))

showed the formation of thick, dense, and crack-free layer of Ni- and Cr-rich particles. The other elements, such as Al, Y, and O particles, showed a dispersed pattern in the coating region. A crack-free coating formed by the NiCrAlY–

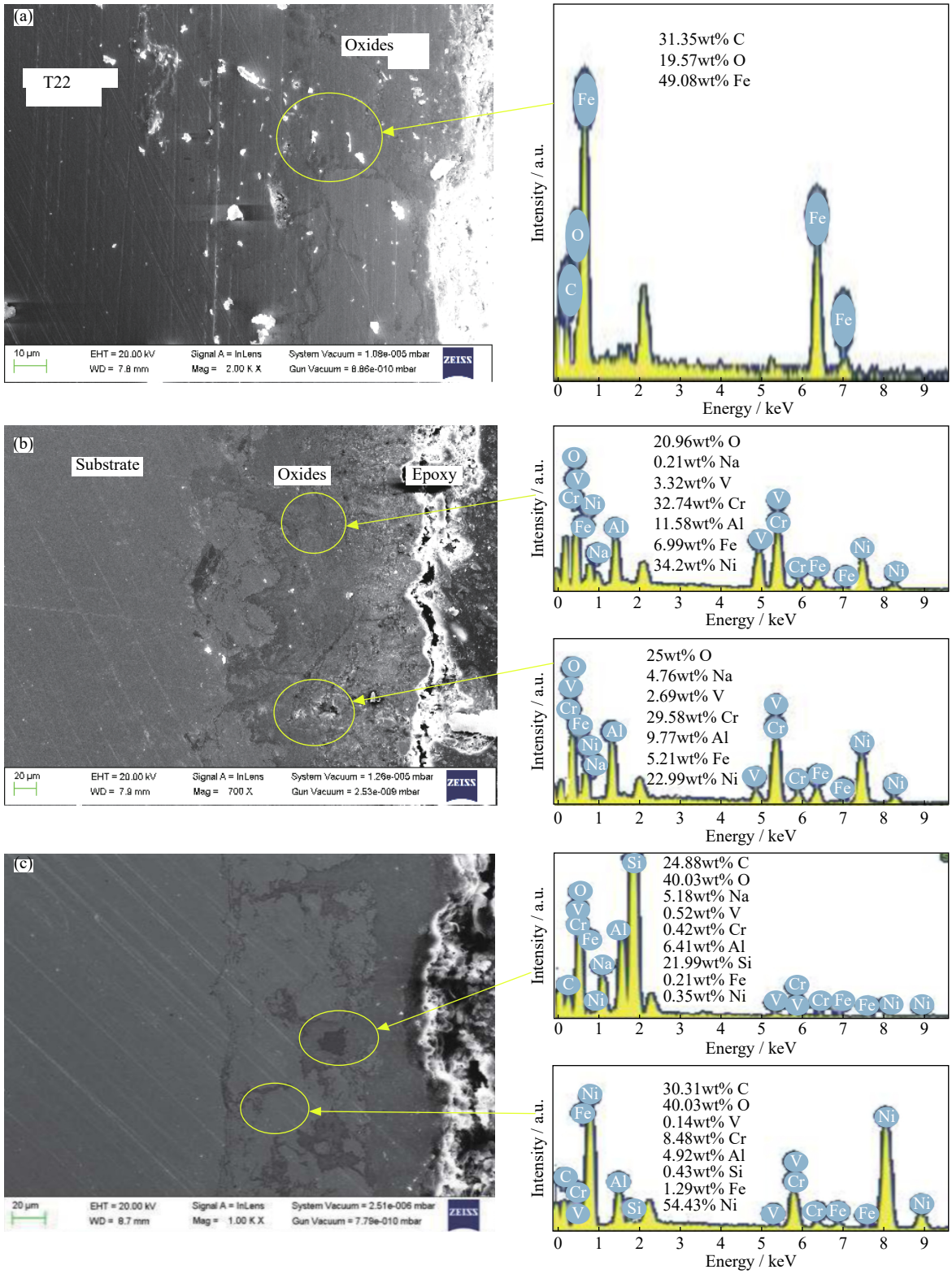

Fig. 14. Cross-sectional SEM/EDS analysis of corroded (a) uncoated T22, (b) NiCrAlY coating, and (c) NiCrAlY–20wt%SiC (N) coating after 50 hot corrosion cycles.

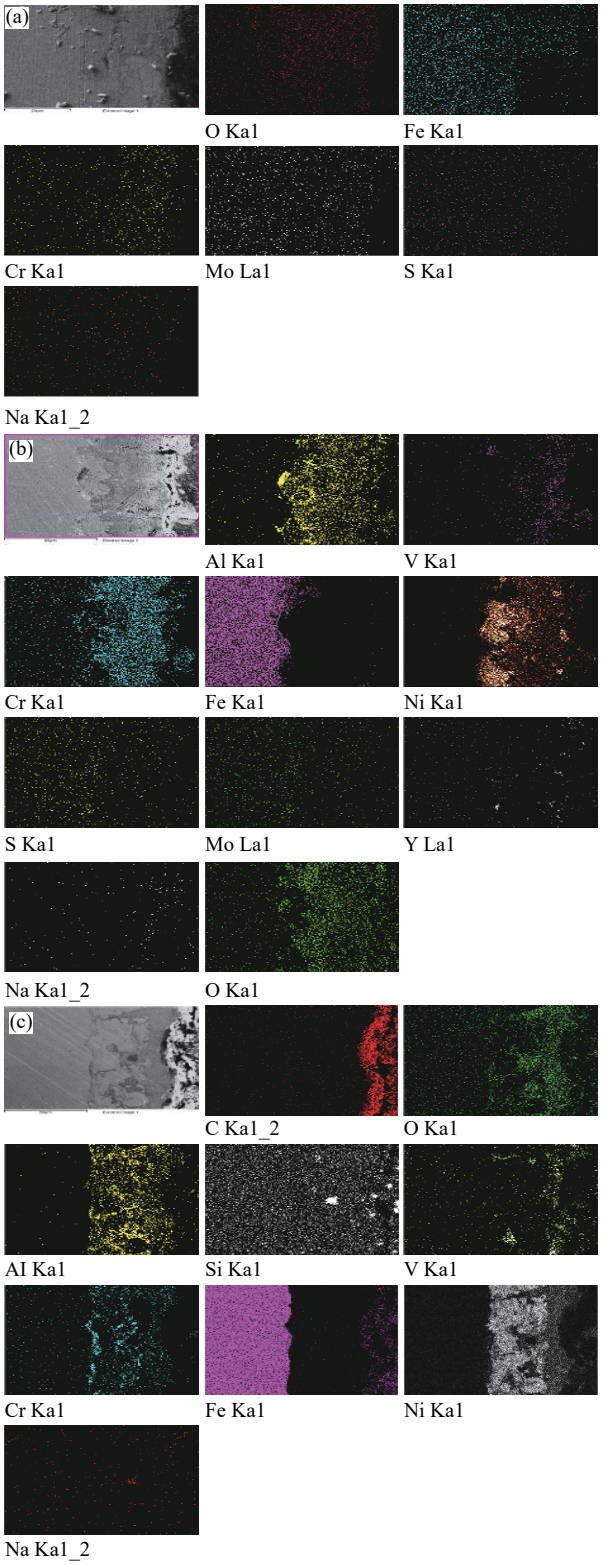

Fig. 15. EDS mapping analysis of corroded (a) uncoated T22, (b) NiCrAlY coating, and (c) NiCrAlY-20wt%SiC (N) coating after 50 hot corrosion cyclbottomes.

20wt%SiC (N) powder consisted of tightly packed splats. The EDS map (Fig. 8(b)) confirmed that the coating primarily mainly constituted of Ni- and Cr-rich splats. Si-rich particles were observed as clots on the metal–coating interface. Uniform distribution of O and C was indicated by the probable formation of oxides and carbides, respectively, in the overall coating and at the interface. Y was uniformly distributed in the overall coating. Al was also observed in several areas. This type of structure formed because of particle fragmentation, flattening of particles, and deformation of splats in the HVOF coatings, as observed by numerous researchers in earlier studies [9–10,34].

For the corrosion in high-temeprature salt condition, Na_2SO_4 and 60% V_2O_5 combined and formed $NaVO_3$ at a temperature of 900°C via the following reaction:

$$Na_2SO_4 + V_2O_5 \rightarrow 2NaVO_3\,(l) + SO_2 + \frac{1}{2}O_2 \qquad (4)$$

The formation of $NaVO_3$, which features a melting point of nearly 610°C, caused the corrosion attack in the form of material spallation of the uncoated steel. Fe_2O_3 formation led to the formation of loosely bound Fe_2O_3 scales, which resulted in a huge mass gain of 217.35 mg/cm^2 after 50 cycles. The weight of oxide continously increased, and the material cracked with a popping sound in the form of flakes in the furnace boats. The Fe_2O_3 development was considered as non-protective over the surface of Fe-based alloys in Na_2SO_4 atmosphere, which led to severe spalling and peeling of alloy as reported by earlier researchers [35–37]. Such serious deterioration attack was observed during the initial cycles due to spontaneous oxygen reaction cause by oxygen diffusion on both sides of the salt layer as reported by Sidhu and Prakash [38].

The NiCrAlY coating band mainly comprised Al, Ni, and Cr, which fused to form Ni–Al and Ni–Cr intermetallic layers throughout the heating course. The developed oxide scales were a combination of small round grains and several large nodules. Localized corrosion in the form of cracking was only noticed on the top layer. Neither crevice corrosion nor pitting was found. Similar scale cracking occurred due to the mismatch of the coefficients of thermal expansion of coatings in earlier studies [39–40]. A small mass gain (13.08 mg/cm^2) was observed for the NiCrAlY alloy coating.

In hot corrosion mechanism, oxide formations started with Al_2O_3 formation because Al necessitates the oxygen partial pressure [41] and minimum Gibbs free energy of formation [42]. Its integrity endures well, and a slight sulfidation might ensue in the coating by oxide dissolution. Thereafter, Ni particles on the top surface layer could form NiO, which was reported to exhibit poor protection in salty environment. NiO might dissolve and precipitate to a certain extent. NiO can be highly susceptible to hot corrosion in

thermal cycling by the given reaction [43]:

$$NiO + SO_3 \rightarrow NSO_4 \quad (5)$$

A similar effect of hot corrosion involving oxide penetration of sulfates through the NiO layer was reported earlier [3]. Cr accompanied by the presence of O was observed in the middle of the scale, indicating the formation of Cr_2O_3 mid-layer in the oxide scale. The presence of Cr_2O_3 in the layers was considered protective; however, Cr_2O_3 could also be susceptible to cracking and spalling during thermal cycling owing to the scale configuration and stress development during high-temperature corrosion as reported by Stott [44].

However, the Cr_2O_3 phase with a high melting point phase remained thermodynamically stable within 900–950°C because it developed a dense and adherent layer that obstructed oxygen attack with the underneath material layers. The co-presence of Ni, Al, and Cr can form $NiAl_2O_4$ and $NiCr_2O_4$ spinels as given in the following reactions:

$$Ni + 2Al + 2O_2 \rightarrow NiAl_2O_4 \quad (6)$$

$$Ni + 2Cr + 2O_2 \rightarrow NiCr_2O_4 \quad (7)$$

Here, the positive corrosion resistance could improve because of the reaction of Cr_2O_3, which stabilized the melt chemistry by developing Na_2CrO_4 solute and inhibited the dissolution of the protective oxide scale [45–46]. Goward reported this limiting hot corrosion resistance behavior of NiCrAlY-based coatings [47]. The adherence of oxide layer depends on different factors, such as interfacial and scale defects, sulfur segregation at the scale–alloy interface, and alloy strength. Microcracking of the scale occurred due to the presence of different thin-layer phases, which might impose severe strain on the coatings [48]. The red-brown layer formation over the surface indicated the presence of Fe_2O_3. However, the growth of continuous and dense layer of protective NiO, Cr_2O_3, and $NiCr_2O_4$ in the surface scale resulted from hot corrosion.

XRD analysis results revealed that the overall scale involved SiO formation along with Al_2O_3, Cr_2O_3, NiO, and spinel $NiCr_2O_4$ phases in their microstructure. The EDS analysis results also confirmed the presence of C and O with all elements of composition, which can promote the development of compounds, such as SiO, SiC, Al_2O_3, Cr_2O_3, NiO, and spinel $NiCr_2O_4$ phases. Gupta and Duvall [49] reported that Si additions in the NiCrAlY coatings enhanced their performance in high-temperature applications, especially in coating adherence. The creation of SiO_2 might have occurred by the two modes of oxidation of SiC by following the primary reaction (active oxidation):

$$SiC(s) + O_2(g) \rightarrow SiO(g) + CO(g) \quad (8)$$

The SiO produced here could be easily vaporized during hot corrosion.

However, the second mode (passive oxidation) can occur through the given reaction:

$$2SiC(s) + 3O_2(g) \rightarrow 2SiO_2(s) + 2CO(g) \quad (9)$$

The SiO_2 development in passive oxidation was relatively stable on the surface and restricted further oxidation because of its high melting point [50]. Certain amounts of SiO_2 could dissolve in basic oxides, e.g., Na_2O scale, to form silicates as proposed by Smialek and Jacobson [51].

$$SiO_2 + Na_2O \rightarrow Na_2SiO_3(l) \quad (10)$$

However, the SiO_2 oxide layer in the coatings is glassy in nature, and it has been considered to possess protective properties, which restrict further inward diffusion of oxide. The protection by this glassy SiO_2 layer has been observed by Tului *et al.* [22], Ouyang *et al.* [23], and Fu *et al.* [52] for Si-based composite coatings. The coating showed the highest corrosion-resistant results with a small final mass gain (1.85 mg/cm^2). The K_P value of NiCrAlY–20wt%SiC (N) coating was the minimum, which renders it a better corrosion-resistant material than its counterpart. The SiO_2 formation in the composite coating intersplats in the subsurface helped in obtaining desirable results against hot corrosion.

5. Conclusions

The following conclusions can be drawn based on the microstructure analysis of the coated surface and hot corrosion behavior of coated and uncoated T22 surface:

(1) Both NiCrAlY and NiCrAlY–20wt%SiC (N) coatings were successfully deposited by the HVOF process, maintaining the composition of the feedstock powders. During the deposition process, minor oxidation was noticed along with negligible decarburization.

(2) During the hot corrosion study, both coated surfaces showed comparatively lesser oxide mass gains than the uncoated surface. The total decrease in mass gain reached 93.98% for the NiCrAlY coating and 99.15% for the NiCrAlY–20wt%SiC (N) coating compared with the uncoated substrate. The mass change kinetics followed the parabolic rate law during the cyclic study for all surfaces.

(3) The protective oxides, including Cr_2O_3, Al_2O_3, NiO, and spinel formations, enhanced the corrosion resistance of the alloy surface. Furthermore, the composite coating offered more shielding against corrosion compared with the alloy coating due to the formation of SiO_2 along with other oxides.

Acknowledgements

The authors thankfully acknowledge IKGPTU, Jaland-

har (Punjab) for their help in carrying out this experimental research. The authors also appreciatively acknowledge DST, New Delhi for their research grant (No. SB/FTP/ETA-435/2012, Dated-10/6/2013) that funded the research and development of the project entitled "Nano-composite Coatings to Control Erosion of Boiler Tubes of Steam Generating Plants."

References

[1] N. Eliaz, G. Shemesh, and R.M. Latanision, Hot corrosion in gas turbine components, *Eng. Fail. Anal.*, 9(2002), No. 1, p. 31.

[2] K. Yamada, Y. Tomono, J. Morimoto, Y. Sasaki, and A. Ohmori, Hot corrosion behavior of boiler tube materials in refuse incineration environment, *Vacuum*, 65(2002), No. 3-4, p. 533.

[3] R.A. Rapp, Hot corrosion of materials: A fluxing mechanism?, *Corros. Sci.*, 44(2002), No. 2, p. 209.

[4] S. Kamal, R. Jayaganthan, and S. Prakash, High temperature cyclic oxidation and hot corrosion behaviours of superalloys at 900°C, *Bull. Mater. Sci.*, 33(2010), No. 3, p. 299.

[5] H. Singh, D. Puri, and S. Prakash, An overview of Na_2SO_4 and/or V_2O_5 induced hot corrosion of Fe- and Ni-based superalloys, *Rev. Adv. Mater. Sci.*, 16(2007), No. 1-2, p. 27.

[6] G.A. Kolta, I.F. Hewaidy, and N.S. Felix, Reactions between sodium sulphate and vanadium pentoxide, *Thermochim. Acta*, 4(1972), No. 2, p. 151.

[7] G.W. Goward, Protective coatings–Purpose, role, and design, *Mater. Sci. Technol.*, 2(1986), No. 3, p. 194.

[8] C. Wagner, Oxidation of alloys involving noble metals, *J. Electrochem. Soc.*, 103(1956), No. 10, p. 571.

[9] T.S. Sidhu, R.D. Agrawal, and S. Prakash, Hot corrosion of some superalloys and role of high-velocity oxy-fuel spray coatings—A review, *Surf. Coat. Technol.*, 198(2005), No. 1-3, p. 441.

[10] Y. Wang and W. Chen, Microstructures, properties and high-temperature carburization resistances of HVOF thermal sprayed NiAl intermetallic-based alloy coatings, *Surf. Coat. Technol.*, 183(2004), No. 1, p. 18.

[11] G. Marginean and D. Utu, Cyclic oxidation behaviour of different treated CoNiCrAlY coatings, *Appl. Surf. Sci.*, 258(2012), No. 20, p. 8307.

[12] L. Ajdelsztajn, J.A. Picas, G.E. Kim, F.L. Bastian, J. Schoenung, and V. Provenzano, Oxidation behavior of HVOF sprayed nanocrystalline NiCrAlY powder, *Mater. Sci. Eng. A*, 338(2002), No. 1-2, p. 33.

[13] Y.N. Wu, M. Qin, Z.C. Feng, Y. Liang, C. Sun, and F.H. Wang, Improved oxidation resistance of NiCrAlY coatings, *Mater. Lett.*, 57(2003), No. 16-17, p. 2404.

[14] L.J. Zhu, S.L. Zhu, and F.H. Wang, Hot corrosion behaviour of a Ni + CrAlYSiN composite coating in Na_2SO_4–25wt%NaCl melt, *Appl. Surf. Sci.*, 268(2013), p. 103.

[15] W.Z. Li, Y. Yao, Q.M. Wang, Z.B. Bao, J. Gong, C. Sun, and X. Jiang, Improvement of oxidation-resistance of NiCrAlY coatings by application of CrN or CrON interlayer, *J. Mater. Res.*, 23(2008), No. 2, p. 341.

[16] H.R. Eschnauer and O. Knotek, Complex carbide powders for plasma spraying, *Thin Solid Films*, 45(1977), No. 2, p. 287.

[17] J. Mehta, V.K. Mittal, and P. Gupta, Role of thermal spray coatings on wear, erosion and corrosion behavior?: A review, *J. Appl. Sci. Eng.*, 20(2017), No. 4, p. 445.

[18] J. Wang, K. Li, D. Shu, X. He, B.D. Sun, Q.X. Guo, M. Nishio, and H. Ogawa, Effects of structure and processing technique on the properties of thermal spray WC–Co and NiCrAl/WC–Co coatings, *Mater. Sci. Eng. A*, 371(2004), No. 1-2, p. 187.

[19] Q. Li, G.M. Song, Y.Z. Zhang, T.C. Lei, and W.Z. Chen, Microstructure and dry sliding wear behavior of laser clad Ni-based alloy coating with the addition of SiC, *Wear*, 254(2003), No. 3-4, p. 222.

[20] Y. Zhou, H. Zhang, and B. Qian, Friction and wear properties of the co-deposited Ni–SiC nanocomposite coating, *Appl. Surf. Sci.*, 253(2007), No. 20, p. 8335.

[21] F. Mubarok and N. Espallargas, Tribological behaviour of thermally sprayed silicon carbide coatings, *Tribol. Int.*, 85(2015), p. 56.

[22] M. Tului, B. Giambi, S. Lionetti, G. Pulci, F. Sarasini, and T. Valente, Silicon carbide-based plasma sprayed coatings, *Surf. Coat. Technol.*, 207(2012), p. 182.

[23] T.Y. Ouyang, S.H. Xiong, Y. Zhang, D.W. Liua, X.W. Fang, Y. Wang, S.J. Feng, T. Zhou, and J.P. Suo, Cyclic oxidation behavior of SiC-containing self-healing TBC systems fabricated by APS, *J. Alloys Compd.*, 691(2017), p. 811.

[24] M. Roy, A. Pauschitz, J. Bernardi, T. Koch, and F. Franek, Microstructure and mechanical properties of HVOF sprayed nanocrystalline Cr_3C_2–25 ($Ni_{20}Cr$) coating, *J. Therm. Spray Technol.*, 15(2006), No. 3, p. 372.

[25] L. Pawlowski, Finely grained nanometric and submicrometric coatings by thermal spraying: A review, *Surf. Coat. Technol.*, 202(2008), No. 18, p. 4318.

[26] M.H. Enayati, F. Karimzadeh, M. Tavoosi, B. Movahedi, and A. Tahvilian, Nanocrystalline NiAl coating prepared by HVOF thermal spraying, *J. Therm. Spray Technol.*, 20(2011), No. 3, p. 440.

[27] T. Grosdidier, A. Tidu, and H.L. Liao, Nanocrystalline Fe-40Al coating processed by thermal spraying of milled powder, *Scripta Mater.*, 44(2001), No. 3, p. 387.

[28] C. Suryanarayana, Synthesis of nanocomposites by mechanical alloying, *J. Alloys Compd.*, 509(2011), p. S229.

[29] D.L. Zhang, Processing of advanced materials using high-energy mechanical milling, *Prog. Mater. Sci.*, 49(2004), No. 3-4, p. 537.

[30] G. Xanthopoulou, A. Marinou, G. Vekinis, A. Lekatou, and M.Vardavoulias, Ni–Al and NiO–Al composite coatings by combustion-assisted flame spraying, *Coatings*, 4(2014), No. 2, p. 231.

[31] M. Oksa, E. Turunen, T. Suhonen, T. Varis, and S.P. Hannula, Optimization and characterization of high velocity

oxy-fuel sprayed coatings: Techniques, materials, and applications, *Coatings*, 1(2011), No. 1, p. 17.

[32] T. Sundararajan, S. Kuroda, T. Itagaki, and F. Abe, Steam oxidation resistance of Ni–Cr thermal spray coatings on 9Cr–1Mo steel. Part 2: 50Ni–50Cr, *ISIJ Int.*, 43(2003), No. 1, p. 104.

[33] N.F. Ak, C. Tekmen, I. Ozdemir, H.S. Soykan, and E. Celik, NiCr coatings on stainless steel by HVOF technique, *Surf. Coat. Technol.*, 174-175(2003), p. 1070.

[34] A.H. Dent, A.J. Horlock, D.G. McCartney, and S.J. Harris, The corrosion behavior and microstructure of high-velocity oxy-fuel sprayed nickel-base amorphous/nanocrystalline coatings, *J. Therm. Spray Technol.*, 8(1999), No. 3, p. 399.

[35] D. Das, R. Balasubramaniam, and M.N. Mungole, Hot corrosion of Fe_3Al, *J. Mater. Sci.*, 37(2002), No. 6, p. 1135.

[36] N. Bala, H. Singh, and S. Prakash, Accelerated hot corrosion studies of cold spray Ni–50Cr coating on boiler steels, *Mater. Des.*, 31(2010), No. 1, p. 244.

[37] T.S. Sidhu, S. Prakash, and R.D. Agrawal, Performance of high-velocity oxy fuel-sprayed coatings on an Fe-based superalloy in Na_2SO_4–60% V_2O_5 environment at 900°C Part II: Hot corrosion behavior of the coatings, *J. Mater. Eng. Perform.*, 15(2006), No. 1, p. 130.

[38] B.S. Sidhu and S. Prakash, Evaluation of the corrosion behaviour of plasma-sprayed Ni_3Al coatings on steel in oxidation and molten salt environments at 900°C, *Surf. Coat. Technol.*, 166(2003), No. 1, p. 89.

[39] S. Danyluk and J.Y. Park, Corrosion and grain boundary penetration in type 316 stainless steel exposed to a coal gasification environment, *Corrosion*, 35(1979), No. 12, p. 575.

[40] P. Niranatlumpong, C.B. Ponton, and H.E. Evans, The failure of protective oxides on plasma-sprayed NiCrAlY overlay coatings, *Oxid. Met.*, 53(2000), No. 3-4, p. 241.

[41] H. Yamano, K. Tani, Y. Harada, and T. Teratani, Oxidation control with chromate pretreatment of MCrAlY unmelted particle and bond coat in thermal barrier system, *J. Therm. Spray Technol.*, 17(2008), No. 2, p. 275.

[42] F. Tang, L. Ajdelsztajn, and J.M. Schoenung, Characterization of oxide scales formed on HVOF NiCrAlY coatings with various oxygen contents introduced during thermal spraying, *Scripta Mater.*, 51(2004), No. 1, p. 25.

[43] A. Andersen, B. Haflan, P. Kofstad, and P.K. Lillerud, High temperature corrosion of nickel and dilute nickel-based alloys in $(SO_2–O_2)/SO_3$ mixtures, *Mater. Sci. Eng.*, 87(1987), p. 45.

[44] F.H. Stott, Developments in understanding the mechanisms of growth of protective scales on high-temperature alloys, *Mater. Charact.*, 28(1992), No. 3, p. 311.

[45] N.S. Bornstein, M.A. DeCrescente, and H.A. Roth, The relationship between relative oxide ion content of Na_2SO_4, the presence of liquid metal oxides and sulfidation attack, *Metall. Trans.*, 4(1973), No. 8, p. 1799.

[46] J.A. Goebel, F.S. Pettit, and G.W. Goward, Mechanisms for the hot corrosion of nickel-base alloys, *Metall. Trans.*, 4(1973), No. 1, p. 261.

[47] G.W. Goward, Progress in coatings for gas turbine airfoils, *Surf. Coat. Technol.*, 108(1998), p. 73.

[48] S. Kamal, K.V. Sharma, and A.M. Abdul-Rani, Hot corrosion behavior of superalloy in different corrosive environments, *J. Miner. Mater. Charact. Eng.*, 3(2015), p. 26.

[49] D.K. Gupta and D.S. Duvall, A silicon and hafnium modified plasma sprayed MCrAlY coating, *Superalloys*, 1984, p. 711.

[50] J. Roy, S. Chandra, S. Das, and S. Maitra, Oxidation behaviour of silicon carbide—A review, *Rev. Adv. Mater. Sci.*, 38(2014), p. 29.

[51] J.L. Smialek and N.S. Jacobson, Mechanism of strength degradation for hot corrosion of α-SiC, *J. Am. Ceram. Soc.*, 69(1986), No. 10, p. 741.

[52] Q.G. Fu, H.J. Li, X.H. Shi, K.Z. Li, and G.D. Sun, Silicon carbide coating to protect carbon/carbon composites against oxidation, *Scripta Mater.*, 52(2005), No. 9, p. 923.